

# An Unsupervised Learning Model for Deformable Medical Image Registration

Guha Balakrishnan  
MIT  
balakg@mit.edu

Amy Zhao  
MIT  
xamyzhao@mit.edu

Mert R. Sabuncu  
Cornell University  
sabuncu@cornell.edu

John Guttag  
MIT  
guttag@mit.edu

Adrian V. Dalca  
MIT and MGH  
adalca@mit.edu

## Abstract

*We present an efficient learning-based algorithm for deformable, pairwise 3D medical image registration. Current registration methods optimize an energy function independently for each pair of images, which can be time-consuming for large data. We define registration as a parametric function, and optimize its parameters given a set of images from a collection of interest. Given a new pair of scans, we can quickly compute a registration field by directly evaluating the function using the learned parameters. We model this function using a CNN, and use a spatial transform layer to reconstruct one image from another while imposing smoothness constraints on the registration field. The proposed method does not require supervised information such as ground truth registration fields or anatomical landmarks. We demonstrate registration accuracy comparable to state-of-the-art 3D image registration, while operating orders of magnitude faster in practice. Our method promises to significantly speed up medical image analysis and processing pipelines, while facilitating novel directions in learning-based registration and its applications. Our code is available at <https://github.com/balakg/voxelmorph>.*

## 1. Introduction

Deformable registration is a fundamental task in a variety of medical imaging studies, and has been a topic of active research for decades. In deformable registration, a dense, non-linear correspondence is established between a pair of  $n$ -D image volumes, such as 3D MR brain scans, depicting similar structures. Most registration methods solve an optimization problem for each volume pair that aligns voxels with similar appearance while enforcing smoothness

constraints on the registration mapping. Solving this optimization is computationally intensive, and therefore extremely slow in practice.

In contrast, we propose a novel registration method that learns a warp function from a collection of volumes. We model the registration function using a convolutional neural network (CNN), that takes two  $n$ -D input volumes and outputs a mapping of all voxels of one volume to another volume. The function is parameterized by network weights that are learned using a training set of volume pairs from the dataset of interest. By sharing the weights over a population, the procedure learns a common representation which can align any new pair of volumes from the same distribution. Registration between a new test scan pair is achieved by simply evaluating the learned function on the given volumes, resulting in rapid registration.

The novelty of our approach is that:

- we propose a learning based solution, and require no supervised information such as ground truth correspondences or anatomical landmarks during training,
- we define registration as a function with parameters shared across a population, enabling registration to be achieved through a function evaluation, and
- our method enables parameter optimization for a variety of cost functions, which can be adapted to various tasks.

Throughout this paper, we use the example of registering 3D MR brain scans. However, our method is broadly applicable to registration tasks, both within and beyond the medical imaging domain. We evaluate our method on a multi-study dataset of over 7,000 scans containing images of healthy and diseased brains from a variety of age groups. Results show that our method achieves comparable accuracy to a state-of-the-art registration package, while taking

orders of magnitude less time. Scans that used to take two hours to register can now be registered within one or two minutes using a CPU, and under a second with a GPU. This is of significant practical importance for many medical image analysis tasks.

## 2. Background

In the typical volume registration formulation, one (moving or source) volume is warped to align with a second (fixed or target) volume. Deformable registration strategies separate an initial affine transformation for global alignment from a typically much slower deformable transformation with higher degrees of freedom. We concentrate on the latter step, in which we compute a dense, nonlinear correspondence for all voxels. Fig. 1 shows sample 2D coronal slices taken from 3D MRI volumes, with boundaries of several anatomical structures outlined. There is significant variability across subjects, caused by differences in health state and natural anatomical variations in healthy brains. Deformable registration enables comparison of structures across scans and population analyses. Such analyses are useful for understanding variability across populations or the evolution of brain anatomy over time for individuals with disease.

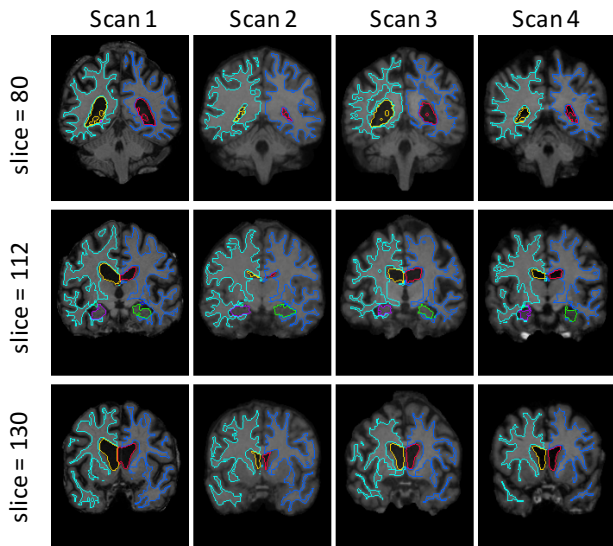


Figure 1: Example coronal slices from the 3D MRI brain dataset, after affine alignment. Each column is a different scan (subject) and each row is a different coronal slice. Several significant anatomical regions are outlined using different colors: L/R white matter in light/dark blue, L/R ventricles in yellow/red, and L/R hippocampi in purple/green. There are significant structural differences across scans, necessitating a deformable registration step to analyze inter-scan variations.

Most existing registration algorithms iteratively optimize a transformation based on an energy function. Let  $F, M$  denote the fixed and moving images, respectively, and  $\phi$  the warp field. The energy function is typically of the form:

$$\mathcal{L}(F, M, \phi) = \mathcal{L}_{sim}(F, M(\phi)) + \lambda \mathcal{L}_{smooth}(\phi), \quad (1)$$

where  $M(\phi)$  denotes  $M$  warped by  $\phi$ , function  $\mathcal{L}_{sim}$  measures image similarity between  $M(\phi)$  and  $F$ , and  $\mathcal{L}_{smooth}$  imposes regularization constraints on  $\phi$ . There are several common formulations for  $\phi$ ,  $\mathcal{L}_{sim}$  and  $\mathcal{L}_{smooth}$ . Often,  $\phi$  is a displacement vector field, specifying the vector offset from  $F$  to  $M$  for each voxel. Diffeomorphic transforms are a popular alternative that model  $\phi$  as the integral of a velocity vector field. As a result, they are able to preserve topology and enforce invertibility on  $\phi$ . Common metrics used for  $\mathcal{L}_{sim}$  include mean squared voxel difference, mutual information, and cross-correlation. The latter two are particularly useful when volumes have varying intensity distributions and contrasts.  $\mathcal{L}_{smooth}$  enforces a spatially smooth deformation, often modeled as a linear operator on spatial gradients of  $\phi$ . In our work, we optimize function parameters to minimize the expected energy of the form of (1) over a dataset of volume pairs, instead of doing it for each pair independently.

## 3. Related Work

### 3.1. Medical Image Registration (Non-learning-based)

There is extensive work in 3D medical image registration<sup>1</sup> [2, 4, 6, 7, 13, 18, 42]. Several studies optimize within the space of displacement vector fields. These include elastic-type models [6, 38], statistical parametric mapping [3], free-form deformations with b-splines, [37] and Demons [42]. Our model also assumes displacement vector fields. Diffeomorphic transforms, which are topology-preserving, have shown remarkable success in various computational anatomy studies. Popular formulations include Large Diffeomorphic Distance Metric Mapping (LDDMM) [7], DARTEL [2] and standard symmetric normalization (SyN) [4].

### 3.2. Medical Image Registration (Learning-based)

There are several recent papers proposing neural networks to learn a function for medical image registration. Most of these rely on ground truth warp fields or segmentations [26, 35, 39, 45], a significant drawback compared to our method, which does not require either. Two recent works [14, 27] present unsupervised methods that are closer to our approach. Both propose a neural network consisting of a CNN and spatial transformation function [23] that

<sup>1</sup>in medical imaging literature, the volumes produced by 3D imaging techniques are often referred to as images

warps images to one another. Unfortunately, these methods are preliminary and have significant drawbacks: they are only demonstrated on limited subsets of volumes, such as 3D subregions or 2D slices, and support only small transformations. [14] employ regularization only implicitly determined by interpolation methods. In contrast, our generalizable method is applicable to entire 3D volumes, handles large deformations, and enables any differentiable cost function. We present a rigorous analysis of our method, and demonstrate results on full MR volumes.

### 3.3. 2D Image Alignment

Optical flow estimation is an analogous problem to 3D volume registration for 2D images. Optical flow algorithms return a dense displacement vector field depicting small displacements between a 2D image pair. Traditional optical flow approaches typically solve an optimization problem similar to (1) using variational methods [8, 21, 41]. Extensions that better handle large displacements or dramatic changes in appearance include feature-based matching [9, 28] and nearest neighbor fields [10].

Several learning-based approaches to dense 2D image alignment have been proposed. One study learns a low-dimensional basis for optical flow in natural images using PCA [44]. Other recent studies in optical flow learn a parametric function using convolutional neural networks [16, 43]. Unfortunately, these methods require ground truth registrations during training. Researchers introduced a spatial transform layer to enable neural networks to perform global parametric 2D image alignment without requiring supervised labels [23]. The technique has since been used for dense spatial transformations as well [34, 46]. We extend the spatial transformer to the 3D setting in our work.

## 4. Method

Let  $F, M$  be two image volumes defined over a  $n$ -D spatial domain  $\Omega \subset \mathcal{R}^n$ . For the remainder of this paper, we focus on the case  $n = 3$ . For simplicity we assume that  $F$  and  $M$  contain single-channel, grayscale data. We also assume that  $F$  and  $M$  are affinely aligned as a preprocessing step, so that the only source of misalignment between the volumes is nonlinear. Many packages are available for rapid affine alignment.

We model a function  $g(F, M; \theta, \lambda) = \phi$  using a convolutional neural network (CNN), where  $\phi$  is a registration field,  $\theta$  are learnable parameters of  $g$ , and  $\lambda$  is a regularization parameter. For each voxel  $p \in \Omega$ ,  $\phi(p)$  is a location such that  $F(p)$  and  $M(\phi(p))$  define similar anatomical locations.

Fig. 2 presents an overview of our method. Our network takes  $M$  and  $F$  as input, and computes  $\phi$  based on a set of parameters  $\theta$ , the kernels of the convolutional layers. We warp  $M(p)$  to  $M(\phi(p))$  using a spatial transformation function, enabling the model to evaluate the similarity of  $M(\phi$

and  $F$  and update  $\theta$ . We use batch gradient descent, minimizing the expected loss over a training set:

$$\mathbb{E}_{F^i, M^i \sim p_{data}(F, M)} [\mathcal{L}(F^i, M^i, \phi^i)], \quad (2)$$

where  $p_{data}(\cdot, \cdot)$  is the data distribution of the population and  $\mathcal{L}(\cdot, \cdot, \cdot)$  is a loss as defined in (1). Importantly, we do not require supervised information such as ground truth registration fields or anatomical landmarks in order to train our network. We learn appropriate values for  $\theta$  by training to align a dataset of volume pairs  $\{F^i, M^i\}_{i=1}^N$  from a population. Given an unseen  $M$  and  $F$  from the same population during test time, we obtain a registration by evaluating  $g$ . We describe our model, which we call *VoxelMorph*, in the next sections.

### 4.1. VoxelMorph CNN Architecture

The parametrization of  $g$  is based on a convolutional neural network architecture similar to UNet [36, 22]. The network consists of two components: an encoder-decoder with skip connections that is responsible for generating  $\phi$  given  $M$  and  $F$ , and a spatial transform function that warps  $M$  to  $M(\phi)$  (see Fig. 2). The spatial transform is only applied during training.

Fig. 3 depicts two variants of the proposed architectures that tradeoff between registration accuracy and computation time. Both take a single input formed by concatenating  $M$  and  $F$  into a 2-channel 3D image. In our experiments, the input is of size  $160 \times 192 \times 224 \times 2$ . We apply 3D convolutions followed by Leaky ReLU activations in both the encoder and decoder stages, with a convolutional kernel size of  $3 \times 3 \times 3$ . The convolutional layers capture hierarchical features of the input image pair necessary to estimate the correspondence  $\phi$ . In the encoder, we use strided convolutions to reduce the spatial dimensions in half until the smallest layer is reached. Successive layers of the encoder operate over coarser representations of the input, similar to the image pyramid used in traditional image registration work.

The receptive fields of the convolutional kernels of the smallest layer should be at least as large as the maximum expected displacement between corresponding voxels in  $M$  and  $F$ . The smallest layer applies convolutions over a volume  $(1/16)^3$  the size of the input images. In the decoding stage, we alternate between upsampling, convolutions (followed by Leaky ReLU activations) and concatenating skip connections. Skip connections propagate features learned during the encoding stages directly to layers generating the registration. The output of the decoder,  $\phi$ , is of size  $160 \times 192 \times 224 \times 3$  in our experiments.

Successive layers of the decoder operate on finer spatial scales, enabling precise anatomical alignment. However, these convolutions are applied to the largest image volumes, which is computationally expensive. We explore this tradeoff using two architectures, *VoxelMorph-1* and

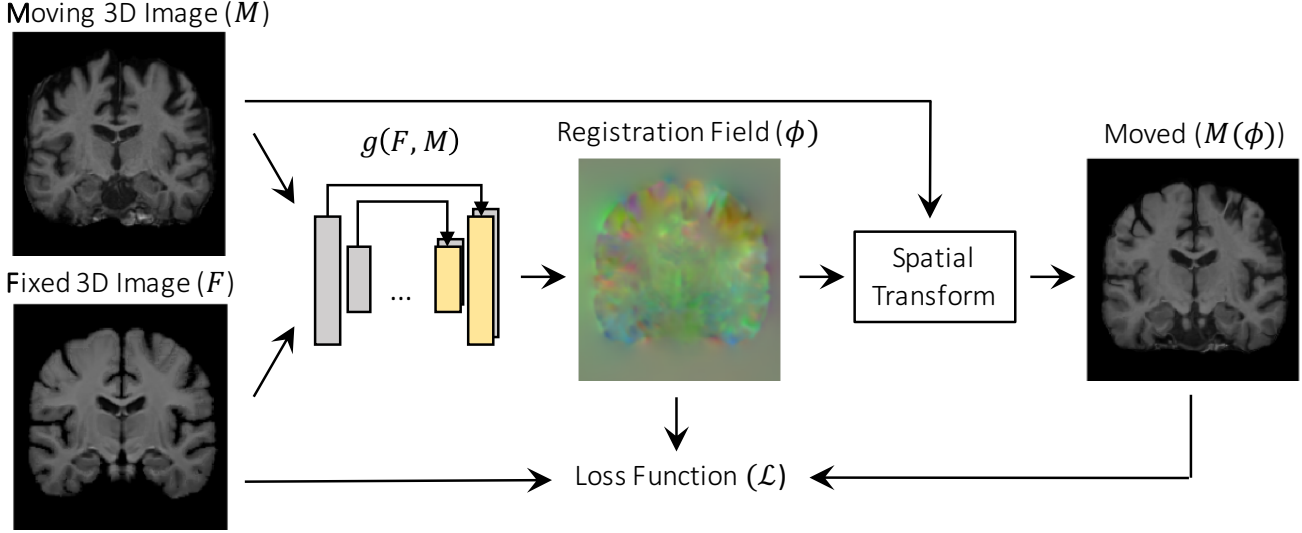


Figure 2: Overview of our method. We learn parameters for a function  $g$  that registers one 3D volume ( $M$ ) to a second, fixed volume ( $F$ ). During training, we warp  $M$  with  $\phi$  using a spatial transformer function. Our loss compares  $M_\phi$  and  $F$  and enforces smoothness of  $\phi$ .

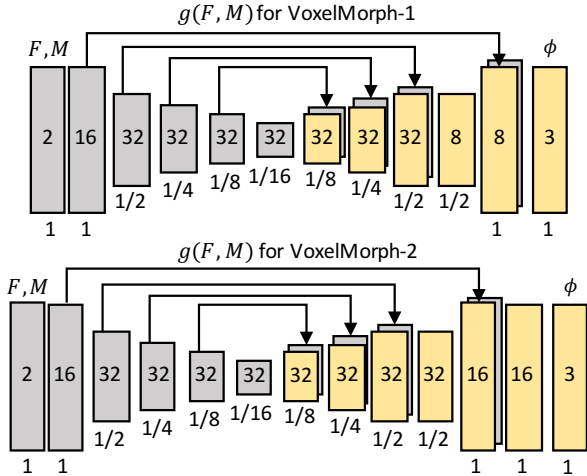


Figure 3: Proposed convolutional architectures implementing  $g(F, M)$ . Each rectangle represents a 3D volume. The number of channels is shown inside the rectangle, and the spatial resolution with respect to the input volume is printed underneath. VoxelMorph-2 uses a larger architecture, using one extra convolutional layer at the output resolution, and more channels for later layers.

VoxelMorph-2, that differ in size at the end of the decoder (see Fig. 3). VoxelMorph-1 uses one less layer at the final resolution and fewer channels over its last three layers.

## 4.2. Spatial Transformation Function

The proposed method learns optimal values in part by minimizing differences between  $M(\phi)$  and  $F$ . In order to use standard gradient-based methods, we construct a differentiable operation based on spatial transformer networks [23] to compute  $M(\phi)$ .

For each voxel  $p$ , we compute a (subpixel) voxel location  $\phi(p)$  in  $M$ . Because image values are only defined at integer locations, we linearly interpolate the values at the eight neighboring voxels. That is, we perform:

$$M(\phi(p)) = \sum_{q \in \mathcal{Z}(\phi(p))} M(q) \prod_{d \in \{x, y, z\}} (1 - |\phi_d(p) - q_d|), \quad (3)$$

where  $\mathcal{Z}(\phi(p))$  refers to the neighbors of  $\phi(p)$ . Because the operations are differentiable, we can backpropagate errors during optimization.

## 4.3. Loss Function

The proposed method works with any differentiable loss. In this section, we formulate an example of a popular loss function  $\mathcal{L}$  of the form (1), consisting of two components:  $\mathcal{L}_{sim}$  that penalizes differences in appearance, and  $\mathcal{L}_{smooth}$  that penalizes local spatial variations in  $\phi$ . In our experiments, we set  $\mathcal{L}_{sim}$  to the negative local cross-correlation of  $M(\phi)$  and  $F$ , which is more robust to intensity variations which can be found across scans and datasets.

Let  $\hat{F}(p)$  and  $\hat{M}(\phi(p))$  denote images with local mean intensities subtracted out. We compute local means over a  $n^3$  volume around each voxel, with  $n = 9$  in our experiments. We write the local cross-correlation (CC) of  $F$  and

$M(\phi)$  as:

$$CC(F, M(\phi)) = \sum_{p \in \Omega} \left[ \frac{\left( \sum_{q \in \mathcal{N}(p)} \hat{F}(q) \hat{M}(\phi(q)) \right)^2}{\left( \sum_{q \in \mathcal{N}(p)} \hat{F}(q)^2 \right) \left( \sum_{q \in \mathcal{N}(p)} \hat{M}(\phi(q))^2 \right) + \epsilon} \right], \quad (4)$$

where  $\epsilon$  is a small constant to avoid numerical issues. A higher CC indicates a better alignment, giving the loss function:  $\mathcal{L}_{sim}(F, M, \phi) = -CC(F, M(\phi))$ . We compute CC efficiently using only convolutional operations over  $M(\phi)$  and  $F$ .

Minimizing  $\mathcal{L}_{sim}$  will encourage  $M(\phi)$  to approximate  $F$ , but may generate a discontinuous  $\phi$ . We encourage a smooth  $\phi$  using a diffusion regularizer on its spatial gradients:

$$\mathcal{L}_{smooth}(\phi) = \sum_{p \in \Omega} \|\nabla \phi(p)\|^2. \quad (5)$$

We approximate spatial gradients using differences between neighboring voxels. The complete loss is therefore:

$$\mathcal{L}(F, M, \phi) = -CC(F, M(\phi)) + \lambda \sum_{p \in \Omega} \|\nabla \phi(p)\|^2, \quad (6)$$

where  $\lambda$  is a regularization parameter.

## 5. Experiments

### 5.1. Dataset

We demonstrate our method on the task of brain MRI registration. We use a large-scale, multi-site, multi-study dataset of 7829 T1weighted brain MRI scans from eight publicly available datasets: ADNI [33], OASIS [29], ABIDE [31], ADHD200 [32], MCIC [19], PPMI [30], HABS [12], and Harvard GSP [20]. Acquisition details, subject age ranges and health conditions are different for each dataset. All scans were resampled to a  $256 \times 256 \times 256$  grid with 1mm isotropic voxels. We carry out standard preprocessing steps, including affine spatial normalization and brain extraction for each scan using FreeSurfer [17], and crop the resulting images to  $160 \times 192 \times 224$ . All MRIs were also anatomically segmented with FreeSurfer, and we applied quality control (QC) using visual inspection to catch gross errors in segmentation results. We use the resulting segmentation maps in evaluating our registration as described below. We split our dataset into 7329, 250, and 250 volumes for train, validation, and test sets respectively, although we highlight that we do not use any supervised information at any stage.

We focus on atlas-based registration, in which we compute a registration field between an atlas, or reference volume, and each volume in our dataset. Atlas-based registration is a common formulation in population analysis, where inter-subject registration is a core problem. The atlas represents a reference, or average volume, and is usually constructed by jointly and repeatedly aligning a dataset of brain MR volumes and averaging them together. We use an atlas computed using an external dataset [17, 40]. Each input volume pair consists of the atlas (image  $F$ ) and a random volume from the dataset (image  $M$ ). Columns 1-2 of Fig. 4 show example image pairs from the dataset using the same fixed atlas for all examples. All figures that depict brains in this paper show 2D coronal slices for visualization purposes only. All registration is done in 3D.

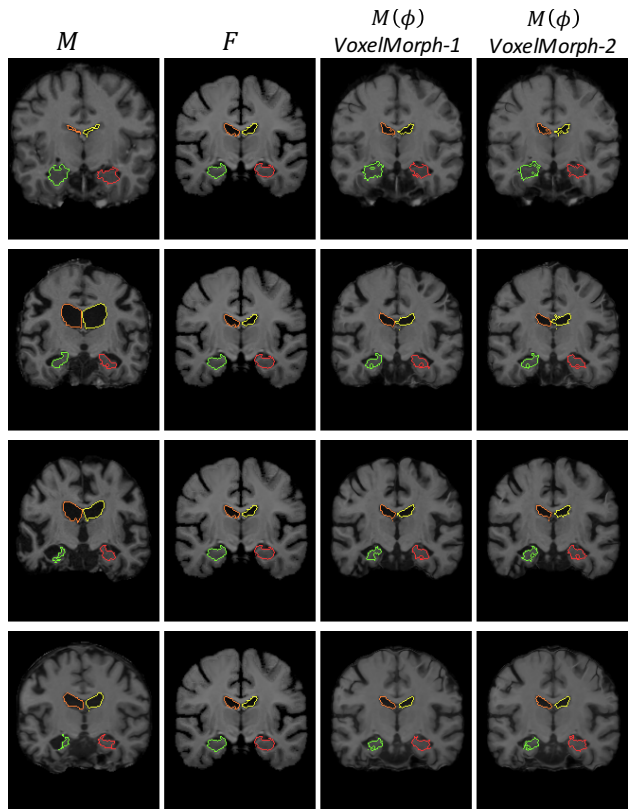


Figure 4: Example MR coronal slices extracted from input pairs (columns 1-2), and resulting  $M(\phi)$  for VoxelMorph-1 and VoxelMorph-2, with overlaid boundaries of the ventricles (yellow, orange) and hippocampi (red, green). A good registration will cause structures in  $M(\phi)$  to look similar to structures in  $F$ . Our networks handle large changes in shapes, such as the ventricles in row 2 and the left hippocampi in rows 3-4.

## 5.2. Dice Score

Obtaining dense *ground truth* registration for these data is not well-defined since many registration fields can yield similar looking warped images. We evaluate our method using expert-labeled anatomical segmentations. We report Dice scores for any anatomical structures that are at least 100 voxels in volume for all test subjects, resulting in 29 structures. If a registration field  $\phi$  represents accurate anatomical correspondences, we expect the regions in  $F$  and  $M(\phi)$  corresponding to the same anatomical structure to overlap well (see Fig. 4 for examples). Let  $S_F^k, S_{M(\phi)}^k$  be the set of voxels of structure  $k$  for  $F$  and  $M(\phi)$ , respectively. We measure the accuracy of our method using the Dice score [15], which quantifies the volume overlap between two structures:

$$\text{Dice}(S_{M(\phi)}^k, S_F^k) = 2 * \frac{S_{M(\phi)}^k \cap S_F^k}{|S_{M(\phi)}^k| + |S_F^k|}. \quad (7)$$

A Dice score of 1 indicates that the sets are identical, and a score of 0 indicates that there is no overlap.

## 5.3. Baseline Methods

We compare our approach to Symmetric Normalization (SyN) [5], the top-performing registration algorithm in a comparative study [25]. We use the SyN implementation in the publicly available ANTs software package [5], with a cross-correlation similarity measure. Throughout our work with medical images, we found the default ANTs smoothness parameters to be sub-optimal for our purposes. We obtained improved parameters using a wide parameter sweep across a multiple of datasets, and use those in these experiments.

## 5.4. Implementation

We implement our networks using Keras [11] with a Tensorflow backend [1]. We use the ADAM optimizer [24] with a learning rate of  $1e^{-4}$ . To reduce memory usage, each training batch consists of one pair of volumes. We train separate networks with different  $\lambda$  values until convergence. We select the network that optimizes Dice score on our validation set, and report results on our held-out test set. Our code and model parameters are available online.<sup>2</sup>

## 5.5. Results

### 5.5.1 Accuracy

Table 1 shows average Dice scores over all subjects and structures for: 1) ANTs, 2) the proposed VoxelMorph architectures, and 3) a baseline of only global affine alignment. VoxelMorph models perform comparably to ANTs, and

Table 1: Average Dice scores and runtime results for affine alignment, ANTs, VoxelMorph-1, VoxelMorph-2. Standard deviations are in parentheses. The average Dice score is computed over all structures and subjects. Timing is computed after preprocessing. Our networks yield comparable results to ANTs in Dice score, while operating orders of magnitude faster during testing. To our knowledge, ANTs does not have a GPU implementation.

Method	Avg. Dice	GPU sec	CPU sec
Affine only	0.567 (0.157)	0	0
ANTs	0.749 (0.135)	-	9059 (2023)
VoxelMorph-1	0.742 (0.139)	0.365 (0.012)	57(1)
VoxelMorph-2	0.750 (0.137)	0.554 (0.017)	144 (1)

VoxelMorph-2 performs slightly better than VoxelMorph-1. All three improve significantly on affine alignment. We visualize the distribution of Dice scores for each structure as boxplots in Fig. 5. For visualization purposes, we combine same structures from the two hemispheres, such as the left and right white matter. The VoxelMorph models achieve comparable Dice measures to ANTs for all structures, performing slightly better than ANTs on some structures such as cerebral white matter, and worse on others such as the hippocampi.

### 5.5.2 Runtime

Table 1 presents runtime results using an Intel Xeon (E5-2680) CPU, and a NVIDIA TitanX GPU. We report the elapsed time for computations following the affine alignment preprocessing step, which all of the presented methods share, and requires just a few minutes on a CPU. ANTs requires roughly two or more hours of CPU time. VoxelMorph-1 and VoxelMorph-2 are 60 and 130+ times faster on average using the CPU. ANTs runtimes vary widely, because its convergence depends on the difficulty of the alignment task. When using the GPU, our networks compute a registration in under a second. To our knowledge, there is no publicly available ANTs implementation for GPUs.

### 5.5.3 Training and Testing on a Subpopulation

The results in the previous sections combine multiple datasets consisting of different population types, resulting in a trained model that generalizes well to a range of subjects. In this section, we model parameters specific to a subpopulation, demonstrating the ability of tailoring our approach to particular tasks. We train using ABIDE subject scans, and evaluate test performance on unseen ABIDE scans. ABIDE contains scans of subjects with autism and controls, and includes a wide age range, with a median age

<sup>2</sup><https://github.com/balagk/voxelmorph>

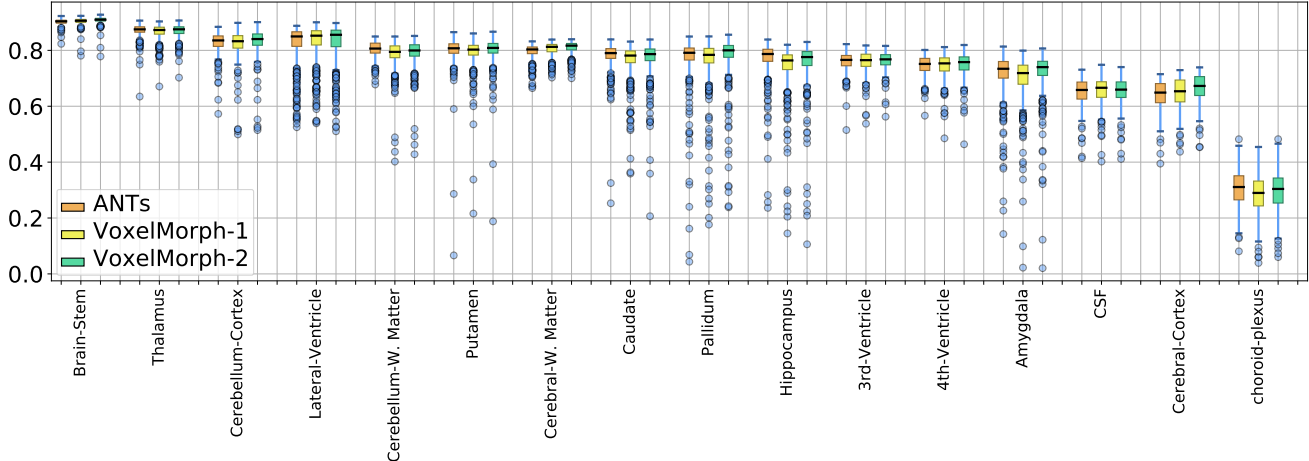


Figure 5: Boxplots of Dice scores for anatomical structures for VoxelMorph-1, VoxelMorph-2 and ANTs. We combine structures with separate left and right brain hemispheres into one structure for this visualization. Structures are ordered by average ANTs Dice score.

of 15 years. In Table 2 we compare the results to those of the models trained on all datasets, presented in the previous section. The dataset-specific networks achieve a 1.5% Dice score improvement.

### 5.5.4 Regularization Analysis

Fig. 6a presents average Dice scores for the validation set for different values of the smoothing parameter  $\lambda$ . As a baseline, we display Dice score of the affinely aligned scans. The optimal Dice scores occur when  $\lambda \approx 1.5$ . However, the results vary slowly over a large range of  $\lambda$  values, showing that our model is robust to choice of  $\lambda$ . Interestingly, even setting  $\lambda = 0$ , which enforces no regularization on registration, results in a significant improvement over affine registration. This is likely due to the fact that the optimal network parameters  $\theta$  need to register all pairs in the training set well, giving an implicit regularization. Fig. 6b shows example registration fields at a coronal slice with different regularization values. For low  $\lambda$ , the field can change dramatically across edges and structural boundaries.

Table 2: Average Dice scores on ABIDE scans, when trained on all datasets (column 2) and ABIDE scans only (column 3). We achieve roughly 1.5% better scores when training on ABIDE only.

Method	Avg. Dice (Train on All)	Avg. Dice (Train on ABIDE)
VoxelMorph-1	0.715(0.140)	0.729(0.142)
VoxelMorph-2	0.718(0.141)	0.734(0.140)

## 6. Discussion

We demonstrate that our model is able to perform on par with the state-of-the-art ANTs registration package while requiring far less computation time to register test volume pairs. While our method learns general features about the data necessary for registration, it can adapt these parameters to specific subpopulations. When training on the ABIDE dataset only, we obtain improved Dice scores on test ABIDE scans compared to training on a dataset from several sources exhibiting different health conditions. This result shows that some of our model’s parameters are learning properties specific to the training images.

We present two models which trade off in accuracy and computation time. The smaller architecture, VoxelMorph-1, runs significantly faster on the CPU and is less than 1 Dice point worse than VoxelMorph-2. This enables an application-specific decision. An advantage of our model is that it is easy to explore this tradeoff by changing the number of convolutional layers and channels of the network, which can be considered as hyperparameters. We selected these hyperparameters by experimenting on training and validation data, but they could be adapted to other tasks.

We quantify accuracy in this study using Dice score, which acts as a proxy measure of registration accuracy. While our models achieve comparable Dice scores, ANTs produces diffeomorphic registrations, which are not guaranteed by our models. Diffeomorphic fields have attractive properties like invertibility and topology-preservation that are useful in some analyses. This presents an exciting area of future work for learning-based registration.

Our network implementations needed a one-time train-

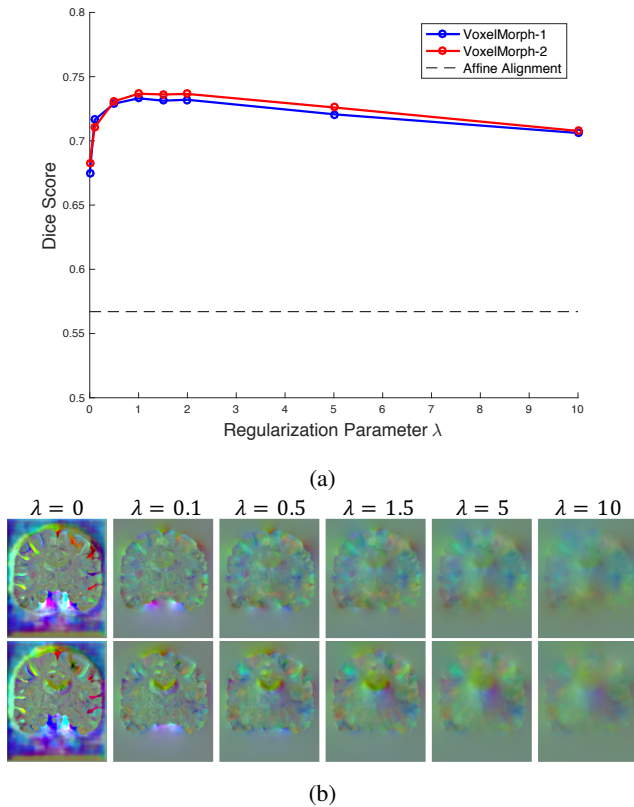


Figure 6: (a) Effect of varying the regularization parameter  $\lambda$  on Dice score. The best results occur when  $\lambda \approx 1.5$ . Also shown are Dice scores when applying only affine registration. (b) Examples of VoxelMorph-2 registration fields for a 2D coronal slice, for different values of  $\lambda$ . Each row is a different scan. We clip the  $x, y, z$  displacements to  $[-10, 10]$ , rescale them to  $[0, 1]$ , and place them in RGB channels. As  $\lambda$  increases, the registration field becomes smoother across structural boundaries.

ing period of a few days on a single NVIDIA TITANX GPU, but less than a second to register a test pair of images. Given the growing availability of image data, our solution is preferable to a non-learning-based approach, and sorely needed to facilitate fast medical image analyses.

## 7. Conclusion

This paper presents an unsupervised learning-based approach to medical image registration, that requires no supervised information such as ground truth registration fields or anatomical landmarks. The approach obtains similar registration accuracy to a popular state-of-the-art 3D image registration package on a large-scale, multi-study MR brain dataset, while operating orders of magnitude faster. Model analysis shows that our model is robust to regulariza-

tion parameter, can be tailored to different data populations, and can be easily modified to explore accuracy and runtime tradeoffs. Our method promises to significantly speed up medical image analysis and processing pipelines, while facilitating novel directions in learning-based registration.

## References

- [1] M. Abadi et al. Tensorflow: Large-scale machine learning on heterogeneous distributed systems. *arXiv preprint arXiv:1603.04467*, 2016. 6
- [2] J. Ashburner. A fast diffeomorphic image registration algorithm. *Neuroimage*, 38(1):95–113, 2007. 2
- [3] J. Ashburner and K. Friston. Voxel-based morphometry—the methods. *Neuroimage*, 11:805–821, 2000. 2
- [4] B. Avants et al. Spatiotemporal normalization for longitudinal analysis of gray matter atrophy in frontotemporal dementia. *Medical Image Computing and Computer-Assisted Intervention (MICCAI)*, 10:303–310, 2007. 2
- [5] B. Avants et al. A reproducible evaluation of ants similarity metric performance in brain image registration. *NeuroImage*, 54(3):2033–2044, 2011. 6
- [6] R. Bajcsy and S. Kovacic. Multiresolution elastic matching. *Computer Vision, Graphics, and Image Processing*, 46:1–21, 1989. 2
- [7] M. F. Beg et al. Computing large deformation metric mappings via geodesic flows of diffeomorphisms. *Int. J. Comput. Vision*, 61:139–157, 2005. 2
- [8] T. Brox et al. High accuracy optical flow estimation based on a theory for warping. *European Conference on Computer Vision (ECCV)*, pages 25–36, 2004. 3
- [9] T. Brox and J. Malik. Large displacement optical flow: Descriptor matching in variational motion estimation. *IEEE Trans. Pattern Anal. Mach. Intell.*, 33(3):500–513, 2011. 3
- [10] Z. Chen et al. Large displacement optical flow from nearest neighbor fields. *IEEE Conf. on Computer Vision and Pattern Recognition (CVPR)*, pages 2443–2450, 2013. 3
- [11] F. Chollet et al. Keras. <https://github.com/fchollet/keras>, 2015. 6
- [12] A. Dagley et al. Harvard aging brain study: dataset and accessibility. *NeuroImage*, 2015. 5
- [13] A. V. Dalca et al. Patch-based discrete registration of clinical brain images. In *International Workshop on Patch-based Techniques in Medical Imaging*, pages 60–67. Springer, 2016. 2
- [14] B. D. de Vos et al. End-to-end unsupervised deformable image registration with a convolutional neural network. In *Deep Learning in Medical Image Analysis and Multimodal Learning for Clinical Decision Support*, pages 204–212. 2017. 2, 3
- [15] L. R. Dice. Measures of the amount of ecologic association between species. *Ecology*, 26(3):297–302, 1945. 6
- [16] A. Dosovitskiy et al. FlowNet: Learning optical flow with convolutional networks. 2015. 3
- [17] B. Fischl. Freesurfer. *Neuroimage*, 62(2):774–781, 2012. 5
- [18] B. Glocker, N. Komodakis, G. Tziritas, N. Navab, and N. Paragios. Dense image registration through mrfs and



- efficient linear programming. *Medical image analysis*, 12(6):731–741, 2008. 2
- [19] R. L. Gollub et al. The mcic collection: a shared repository of multi-modal, multi-site brain image data from a clinical investigation of schizophrenia. *Neuroinformatics*, 11(3):367–388, 2013. 5
- [20] A. J. Holmes et al. Brain genomics superstruct project initial data release with structural, functional, and behavioral measures. *Scientific data*, 2, 2015. 5
- [21] B. K. Horn and B. G. Schunck. Determining optical flow. 1980. 3
- [22] P. Isola et al. Image-to-image translation with conditional adversarial networks. *arXiv preprint*, 2017. 3
- [23] M. Jaderberg et al. Spatial transformer networks. In *Advances in neural information processing systems*, pages 2017–2025, 2015. 2, 3, 4
- [24] D. P. Kingma and J. Ba. ADAM: A method for stochastic optimization. *arXiv preprint arXiv:1412.6980*, 2014. 6
- [25] A. Klein et al. Evaluation of 14 nonlinear deformation algorithms applied to human brain mri registration. *Neuroimage*, 46(3):786–802, 2009. 6
- [26] J. Krebs et al. Robust non-rigid registration through agent-based action learning. In *Medical Image Computing and Computer-Assisted Intervention (MICCAI)*, pages 344–352, Cham, 2017. Springer International Publishing. 2
- [27] H. Li and Y. Fan. Non-rigid image registration using fully convolutional networks with deep self-supervision. *arXiv preprint arXiv:1709.00799*, 2017. 2
- [28] C. Liu et al. SIFT flow: Dense correspondence across scenes and its applications. *IEEE Trans. Pattern Anal. Mach. Intell.*, 33(5):978–994, 2011. 3
- [29] D. S. Marcus et al. Open access series of imaging studies (oasis): cross-sectional mri data in young, middle aged, nondemented, and demented older adults. *Journal of cognitive neuroscience*, 19(9):1498–1507, 2007. 5
- [30] K. Marek et al. The parkinson progression marker initiative. *Progress in neurobiology*, 95(4):629–635, 2011. 5
- [31] A. D. Martino et al. The autism brain imaging data exchange: towards a large-scale evaluation of the intrinsic brain architecture in autism. *Molecular psychiatry*, 19(6):659–667, 2014. 5
- [32] M. P. Milham et al. The ADHD-200 consortium: a model to advance the translational potential of neuroimaging in clinical neuroscience. *Frontiers in systems neuroscience*, 6:62, 2012. 5
- [33] S. G. Mueller et al. Ways toward an early diagnosis in alzheimer’s disease: the alzheimer’s disease neuroimaging initiative (adni). *Alzheimer’s & Dementia*, 1(1):55–66, 2005. 5
- [34] E. Park et al. Transformation-grounded image generation network for novel 3D view synthesis. In *IEEE Conference on Computer Vision and Pattern Recognition (CVPR)*, pages 702–711, 2017. 3
- [35] M.-M. Rohé et al. SVF-Net: Learning deformable image registration using shape matching. In *Medical Image Computing and Computer-Assisted Intervention (MICCAI)*, pages 266–274, Cham, 2017. Springer International Publishing. 2
- [36] O. Ronneberger et al. U-net: Convolutional networks for biomedical image segmentation. In *Medical Image Computing and Computer-Assisted Intervention (MICCAI)*, pages 234–241. Springer, 2015. 3
- [37] D. Rueckert et al. Nonrigid registration using free-form deformation: Application to breast mr images. *IEEE Transactions on Medical Imaging*, 18(8):712–721, 1999. 2
- [38] D. Shen and C. Davatzikos. Hammer: Hierarchical attribute matching mechanism for elastic registration. *IEEE Transactions on Medical Imaging*, 21(11):1421–1439, 2002. 2
- [39] H. Sokooti et al. Nonrigid image registration using multi-scale 3d convolutional neural networks. In *Medical Image Computing and Computer-Assisted Intervention (MICCAI)*, pages 232–239, Cham, 2017. Springer International Publishing. 2
- [40] R. Sridharan et al. Quantification and analysis of large multimodal clinical image studies: Application to stroke. In *International Workshop on Multimodal Brain Image Analysis*, pages 18–30. Springer, 2013. 5
- [41] D. Sun et al. Secrets of optical flow estimation and their principles. *IEEE Conf. on Computer Vision and Pattern Recognition (CVPR)*, pages 2432–2439, 2010. 3
- [42] J. Thirion. Image matching as a diffusion process: an analogy with maxwell’s demons. *Medical Image Analysis*, 2(3):243–260, 1998. 2
- [43] P. Weinzaepfel, J. Revaud, Z. Harchaoui, and C. Schmid. Deepflow: Large displacement optical flow with deep matching. In *IEEE International Conference on Computer Vision (ICCV)*, pages 1385–1392, 2013. 3
- [44] J. Wulff and M. J. Black. Efficient sparse-to-dense optical flow estimation using a learned basis and layers. *IEEE Conf. on Computer Vision and Pattern Recognition (CVPR)*, pages 120–130, 2015. 3
- [45] X. Yang et al. Quicksilver: Fast predictive image registration—a deep learning approach. *NeuroImage*, 158:378–396, 2017. 2
- [46] T. Zhou et al. View synthesis by appearance flow. *European Conference on Computer Vision (ECCV)*, pages 286–301, 2016. 3